Enhanced deep detection of Raman scattered light by wavefront shaping

ALBA M. PANIAGUA-DIAZ,[1] ADRIAN GHITA,[1] TOM VETTENBURG,[1,2] NICK STONE,[1] AND JACOPO BERTOLOTTI[1,*]

[1] University of Exeter, Stocker Road, Exeter EX4 4QL, United Kingdom
[2] University of Dundee, Nethergate, Dundee DD1 4HN, United Kingdom
[*] j.bertolotti@exeter.ac.uk

Abstract: Light scattering limits the penetration depth of non-invasive Raman spectroscopy in biological media. While safe levels of irradiation may be adequate to analyze superficial tissue, scattering of the pump beam reduces the Raman signal to undetectable levels deeper within the tissue. Here we demonstrate how wavefront shaping techniques can significantly increase the Raman signal at depth, while keeping the total irradiance constant, thus increasing the amount of Raman signal available for detection.

1. Introduction

Raman spectroscopy enables label-free identification of chemical composition [1, 2]. This is particularly useful for investigating living biological tissues, where the unique rotational and vibrational modes of organic molecules allow non-invasive detection of physiologically important and disease specific bio-analytes [3]. However, since the spontaneous Raman signal is directly proportional to the pump intensity that decreases rapidly with depth in diffusive media due to multiple-scattering, this limits how far into the tissue a specific molecular target can be detected. Innovative illumination and detection geometries may improve the signal level [4]; however, the amount of light that can reach the target remains a fundamental limit. This effectively confines Raman spectroscopy to surface studies of scattering tissue [5–7].

Although multiple scattering of light in disordered media can appear random, the underlying physics is completely deterministic and relatively well understood [8]. In recent years, wavefront shaping techniques have emerged as a way to manipulate waves, even through strongly scattering media [9, 10]. In particular, wavefront shaping allows the focusing of light at a specific target inside a scattering medium [11]. This makes it possible to concentrate the pump on the Raman active material, even when it is buried deep inside a tissue [12]. The limit of this approach is that wavefront shaping in an unknown multiply scattering structure is typically achieved iteratively, using the signal as a feedback and gradually improving it [13]. As the Raman signal is generally weak, an adequate signal-to-noise ratio requires long integration times. The necessity to repeat the measurement many times makes this approach slow and limits the maximum enhancement achievable. In particular the pioneering work by Thompson et al. achieved an increase of the detected Raman signal by approximately 25%, but required at least 10-20 times the time of a single Raman measurement [12]. Additionally, these approaches are only useful when there is an initial detectable Raman signal, not addressing the problem of blind sensing in scattering media.

In this article we show that wavefront-shaping the pump beam to maximize its penetration depth can overcome the two main limitations of techniques based on light focusing: speed, and compatibility with blind sensing. Given that in this case the feedback is provided by the pump and not the Raman signal, there is no need for prior knowledge of Raman elements. At the same time, due to the much larger intensity of the pump with respect to the Raman signal, the integration time in the detector can be much shorter. This enables full optimization on a much shorter timescale than the typical Raman measurement [14]. We experimentally show an

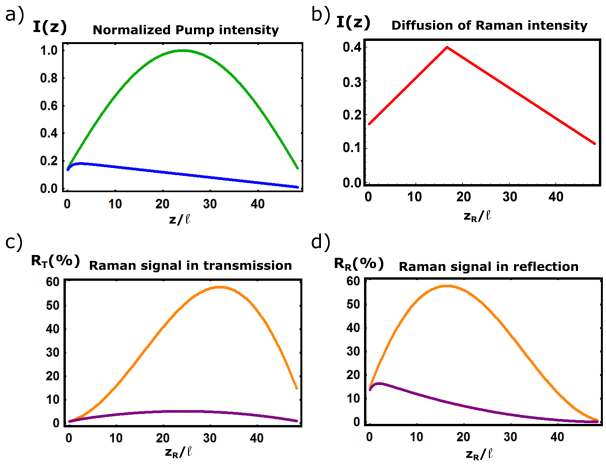

Fig. 1. a) Normalized intensity distribution of the pump light when the beam is not optimized (blue) and when all the incident energy is optimized and coupled to the fundamental solution of the diffusion equation (green). b) Intensity distribution of a point Raman element placed at position $z_R = 10\,\mu$m. c) Raman scattered light in transmission of a target at position z_R/ℓ, when the beam is optimized (orange) and when it is not optimized (purple). d) Raman scattered light in reflection of a target at position z_R/ℓ, when the beam is optimized (orange) and when it is not (purple).

enhancement of approximately 50% through a scattering layer with optical density of ~ 48, and study how the achievable enhancement in depth depends on the target position and the wavefront shaping quality.

2. Pump energy distribution and Raman signal generation

The propagation of light intensity in a scattering medium can be described by the diffusion equation:

$$\frac{dI}{dt} = D\nabla^2 I - \alpha I + S, \tag{1}$$

where S is the source term, α is the absorption coefficient, and D is the diffusion coefficient [8].

In the following we consider a continuous (CW) source, i.e. the steady-state regime of the diffusion equation, and a slab geometry. Furthermore, as we integrate all the intensity along the transverse coordinates, we are only interested in the transport along the z-axis, and Eq. (1) reduces to a one-dimensional equation with Green's function, $g\left(z, z_j\right)$, that satisfies $D\frac{\partial^2}{\partial z^2} g\left(z, z_j\right) - \alpha g\left(z, z_j\right) = -\delta\left(z - z_j\right)$, and is given by:

$$g\left(z, z_j\right) = \frac{H\left(z_j - z\right) e^{\sqrt{\frac{\alpha}{D}}(z - z_j)} + H\left(z - z_j\right) e^{\sqrt{\frac{\alpha}{D}}(z_j - z)}}{2\sqrt{\alpha D}} + C_1 e^{\sqrt{\frac{\alpha}{D}}(z - z_j)} + C_2 e^{-\sqrt{\frac{\alpha}{D}}(z - z_j)}, \tag{2}$$

where H is the Heaviside step function, while C_1 and C_2 are integration constants to be fixed by the boundary conditions.

In our experiment scattering is dominant over absorption (i.e. the transport mean free path of the scattering media, ℓ_t, is shorter than the absorption length). By imposing the conservation of energy fluxes in the medium, one obtains Robin boundary conditions that can be recast as $I = 0$ at a distance from the edge of the sample (the extrapolation lengths z_{e1} and z_{e2}) [15]. When

$\alpha = 0$, the Green's function takes the compact form

$$g(z, z_j) = \frac{I_0}{D}\left(\frac{(z + z_{e1})(L + z_{e2} - z_j)}{L + z_{e2} + z_{e1}} + (z_j - z)H(z - z_j)\right), \tag{3}$$

where I_0 is the total intensity of the pump L is the thickness of the slab.

The intensity profile $I(z)$ inside the diffusive slab is then given by the convolution of g with the source S. There are two source functions that are relevant to the problem we are investigating: an exponentially decaying source $S(z) = e^{-z/z_j}$ due to the exponential decay of ballistic intensity as propagating through the medium (following Lambert-Beer law), and a point source $S(z) = \delta(z - z_j)$, representing the diffusion process of an element originated at a specific position z_j. The intensity of the pump is well described by the exponentially decaying source (blue curve in Fig. 1(a), whereas the intensity originating from a point Raman element, is better described by the point source [Fig. 1(b)]. If the system is absorbing, the Green's function is not composed of two straight lines as in Fig. 1(b), but it consists of two shallow exponentials [8]. However, as long as the absorption length is larger than the transport mean free path, the effect on the energy leakage is insignificant as shown by Yu et al. [16].

Interestingly, the diffusion approximation used to describe light propagation in scattering media does not take into account the fact that light is a wave. However, the multiply scattered light paths inside a disordered medium can interfere, giving rise to a large number of effects, from speckle correlations [17, 18], to the coherent backscattering cone [19, 20]. A particularly interesting wave effect is the presence of "open" channels, i.e. the fact that it doesn't matter how scattering a system is, there is always a small number of possible incident wavefronts such that all back-reflected light interfere destructively and are thus completely transmitted [21, 22]. In contrast to what one may expect, a mode with perfect transmission is not a mode where light traverses the sample unhindered. On the contrary, the mode with the highest transmission is also one that accumulates a large amount of energy inside the sample [23, 24], and the energy is approximately distributed as a cosine with a maximum at the center [25], as shown by the green curve in Fig. 1(a).

As shown in Fig. 1(a), the diffusion approximation and the open channels represent the worst and best case scenarios, respectively. The diffusion solution in a uniform slab (blue curve) has a maximum at about one transport mean free path of depth, but then decreases rapidly with depth, meaning that not much light is able to reach the deepest parts of the medium. In contrast, if one could perform perfect wavefront shaping and couple to an open channel (green curve), the pump distribution would be symmetric and have a maximum at the center. This is a particularly interesting feature, given that when the element to detect is in the central regions of the sample, the pump intensity is generally weak, and consequently it becomes much more difficult to detect Raman signal from there [26]. Realistic or experimental wavefront shaping will produce an intermediate distribution between the open channel and diffusive extremes [24].

Once the pump reaches the Raman-active material, the Raman signal is generated and propagates diffusively to the exit of the sample. For simplicity we assume that the Raman signal is generated by a point source at position z_R, resulting in a distribution of the Raman signal given by Eq. (3) with $z_j = z_R$ [Fig. 1(b)]. The total amount of diffused light intensity that exits the medium is given by its gradient at the interface (Fick's law [27]), so we can define T and R as the intensity coming out from the transmission and reflection side of the slab respectively (normalized to the incident intensity), as [8, 28]:

$$T = -\frac{D}{I_0}\left.\frac{dI(z)}{dz}\right|_{z=L} \quad \text{and} \quad R = \frac{D}{I_0}\left.\frac{dI(z)}{dz}\right|_{z=0}. \tag{4}$$

Using Eq. (4) we can then calculate the total amount of diffuse Raman signal that can be collected in transmission (R_T) and in reflection (R_R) as a function of z_R when the different pumps

are considered [Figs. 1(c)- 1(d)]. As seen in Figs. 1(c)- 1(d), if the Raman active material is very close to the surface of the material there is no real advantage from the wavefront shaping approach. On the other hand, for depths larger than a few transport mean free paths, we expect a significantly higher signal if we wavefront-shape the pump light to maximize transmission, particularly for elements near the center.

3. Wavefront shaping of the pump for maximal transmission

Despite the great interest and efforts put towards fully transmitting the incident light through scattering media (i.e. coupling to the open channels), it has not been achieved experimentally yet, though substantial increases in the transmitted light have been reported [28–31]. The main factor preventing the experimental coupling of light to the open channels is that the scattered electro-magnetic field has more degrees of freedom than can be controlled effectively [16, 32–34]. Hence, even if the theoretical scattering matrix is square and loss-less; in practice, we only have access to a non-Hermitian sub-matrix with losses and coupling between the modes.

The total number of degrees of freedom, N, at the entrance of the sample can be well approximated by the number of diffraction limited spots contained within the illumination area, A, such that: $N \propto \frac{2\pi A}{\lambda^2}$, where λ is the wavelength of the illumination source [31]. In our experimental case, the radius of the illuminated spot at the entrance of the sample is $R = 22\,\mu\text{m}$ and $\lambda = 785\,\text{nm}$, which makes $N \approx 15500$. However, due to the limited degrees of control segments of the spatial light modulator, the number of controlled degrees of freedom at the entrance of the sample is $N_C = 3520$.

The total number of degrees of freedom, M, of the field at the output of the sample can be estimated from the size of the area that the light spreads out over after transmission through the sample. Assuming a 45° diffusion of the incident area of light, the total number of degrees of freedom in the output field can be seen to be approximately $M = 80,000$ for the experimental parameters considered here (Section 4). The optimal transmission enhancement for a system described by a random $M \times N_C$-matrix is given by the square of its largest singular value. Marčenko and Pastur showed that large rectangular random matrices (with normal-distributed random complex elements) have a distribution of singular values that only depends on the ratio, N_C/M, of the number of input and output modes and with finite support [35]. The distribution of singular values indicates a maximum intensity enhancement after optimization of $\left\langle T_{op}/T_{in} \right\rangle = \left(1 + \sqrt{N_C/M}\right)^2$.

Assuming that the transmission matrix is indeed random, we can expect an increase in total transmission by a factor of 1.46. Larger enhancement factors may be possible if the effective number of degrees of freedom that can be controlled in the output field is reduced due to correlations in the output-modes [16, 33]. For the samples considered here, the effective number of output modes is, $M_E = \frac{M}{1+\frac{2M}{3g}} \approx 1.5g = 798$, where $g = 532.18$ is the dimensionless conductance calculated for our experimental geometry [34]. This suggests that, under optimal conditions, enhancements up to a factor of 9.6 would be possible.

4. Materials and methods

The experimental apparatus is shown in Fig. 2. The pump laser (1 W MOPA, Innovative Photonic Solutions) has its central wavelength in the near infrared $\lambda = 785\,\text{nm}$, to achieve larger penetration depth in biological tissue. The wavelength region that allows maximal penetration in the optical regime is approximately between 700 and 900 nm [36, 37] where the absorption band of water has a broad dip. The pump laser is incident on a Digital Micromirror Device (DLP 9500, Texas Instruments) spatial light modulator (SLM) that iteratively adapts the phase profile of the wavefront using a variation of the partitioning algorithm (where approximately 50% of the pixels of the spatial light modulator are changed at a time) [38]. We started by addressing

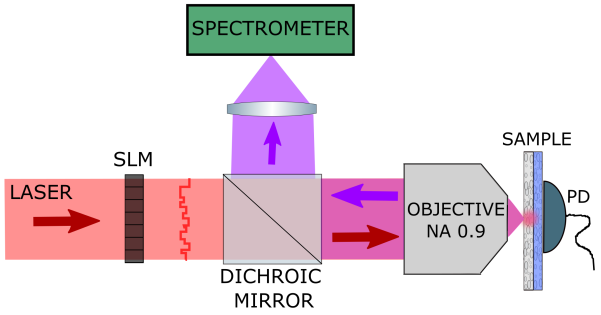

Fig. 2. Schematic of the experimental apparatus used to increase total transmission through a scattering medium whilst the Raman spectra is collected in reflection. Red arrows represent the pump light at 785 nm and the purple arrow represents the longer wavelengths generated due to the spontaneous Raman scattered light.

approximately 20% of the pixels. In order to ensure a high Signal to Noise Ratio (SNR), during the optimization we gradually reduced the percentage of addressed pixels up to 1-2%, given that in a noise-free situation the wavefront will converge faster when individual phase pixels are addressed [38]. Additionally at the beginning of the algorithm we grouped several phase pixels, starting by 8×8, which helps increasing the SNR quickly at the beginning. As the algorithm evolves we reduce the number of grouped pixels up to 1×1, where the size of each pixel on the sample is demagnified, becoming diffraction limited in size. The modulated wavefront is focused on the sample by a microscope objective (NA=0.9, 100x, dry, Leica), achieving a spot size of $44 \pm 12\,\mu$m in diameter. A photo-diode collects the total transmitted light (mainly from the pump) and utilizes it as feedback for an iterative algorithm controlling the SLM [38]. The backscattered Raman signal is filtered by a dichroic mirror (LPD02-785RU, Semrock), together with a long pass filter (LP02-785RU-25, Semrock). After the filtering phase, the Raman light is directed onto a spectrometer (Holospec 1.8i, Kaiser optical) equipped with a high dispersion grating (864 mm, Kaiser Optical) and a NIR CCD detector (Andor iDus 420, Oxford Instruments). The estimated spectral resolution of the system is $1.08\,\mathrm{cm}^{-1}$ with a $25\,\mu$m slit, measured with a calibration atomic line source.

The sample was made of two different materials, a highly scattering layer of anatase TiO_2 (Fisher Scientific UK) of thickness $L = 29 \pm 2\,\mu$m and a second layer of Calcium Hydroxyapatite (HAP) with a thickness of $120 \pm 10\,\mu$m (Sigma Aldrich UK). The layer of TiO_2 was chosen because it is a highly scattering material with very little absorption, which allows us obtain large optical densities with small thicknesses, in this case the optical density is $L/\ell_t \sim 29/0.6 \approx 48$, comparable to thicknesses of ~ 5 cm [36, 37] in fatty biological media, where the transport mean free path is ~ 1 mm (the effect of a thicker sample is considered in the Discussion section). In this article we consider only non-absorbing scattering media; a generalization to absorbing media would modify Eq. (3) introducing an exponential decay of the intensity from the source origin, and would change the shape of the intensity distribution of the open channels [39], but would not change the general physics of the problem [16]. HAP is a calcium phosphate mineral similar to that found in many hard tissues, and of interest for various biomedical applications [40], for instance as a marker to detect calcifications in breast tissue [5]. Fig. 3 shows the Raman spectra for the anatase TiO_2 and HAP materials (panels a and b), and panel c shows the combined spectra collected by the spectrometer in the experimental reflection configuration, where we can see the reduced peak from HAP at around $960\,\mathrm{cm}^{-1}$, attenuated by the TiO_2 layer. The spectra were acquired in 5 accumulations of 10 seconds for each acquisition. The laser power incident on the sample was measured to be 9.7 ± 0.1 mW. After removing the offset intensity from the detector,

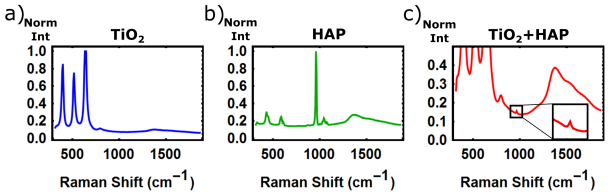

Fig. 3. Normalized Raman spectra of the different materials of the sample: a) Anatase TiO_2 spectrum, with three main peaks at 396,512 a*nd*631 cm^{-1} b) Calcium Hydroxyapatite (HAP) with the main peak at 960 cm^{-1} and c) the collected spectrum of the combined sample of TiO_2 and HAP, where we can see a strong signal coming from the first layer of TiO_2 and a weak peak coming from the inner HAP at 960 cm^{-1}, magnified in the inset. The broad contribution around 1500 cm^{-1} is due to the fluorescence of the microscope cover slide.

the recorded Raman spectra were imported to Mathematica for data post-processing, primarily consisting of background subtraction (third order polynomial). After background subtraction we performed a Lorentzian fit to the peak of interest and normalized the values for simplicity, as shown in Fig. 4. In order to evaluate the increase in the Raman peak of interest, we compare the integrated area under the peak for the optimized and non-optimized wavefronts.

5. Results

Using iterative wavefront shaping techniques we increased the total transmission of the pump light through the scattering medium by a factor of 1.40 ± 0.3. In Fig. 4(a) we show the Raman signal intensity corresponding to the main peak of the subsurface HAP layer, before (red) and after the wavefront optimization (green). The dots represent the experimental data and the solid line curves are Lorentzian fits to the data. It can be seen that the optimization in the pump wavefront results in a 40% stronger Raman scattering signal in that particular measurement, whereas we obtained an enhancement of up to 48% as can be seen in Fig. 4(b).

Both the TiO_2 and the HAP layers are composed by a scattering powder, but since the two refractive indices are very different ($n_{TiO_2} \simeq 2.26, n_{\mathrm{HAP}} \simeq 1.6$) most of the scattering is coming from the TiO_2 layer, and when optimizing the total transmission we are increasing the pump intensity in both layers. As the spontaneous Raman signal is proportional to the pump intensity [41], we expect the increase in the Raman signal collected from the HAP layer to be approximately linear with the increase in the total transmission. In Fig. 4(b) we show the relationship between the increase in total transmission of the pump and the increase in the intensity of the collected Raman signal, for different values of the optimization. The best fit model follows a linear curve of slope 1.07 ± 0.12, showing that to a very good approximation the increase in pump transmission is linear with the increase in the collected Raman intensity.

5.1. Estimated increase in penetration depth

Increasing the amount of generated Raman signal means that one can detect samples from deeper into a scattering medium. To quantify how much, we assume that a Raman active medium at a depth z_R produces an acceptable signal to noise ratio, and normalize the intensity of the signal produced, which will then diffuse, exit the scattering slab, and reach our detector (blue dashed curve in Figs. 5(a) and 5(c). If wavefront shaping of the pump enhances the Raman light produced by a factor β the active medium can be at a deeper position z_R^0 and still produce the same amount of measurable signal, as shown by the solid green curve in Figs. 5(a) and 5(c).

In order to generate the same output Raman signal, with intensity distribution $I(z = z_R)$ given by Eqs. (3) and (4), the two distributions of intensity must have the same gradient $\tan(\alpha)$ at the

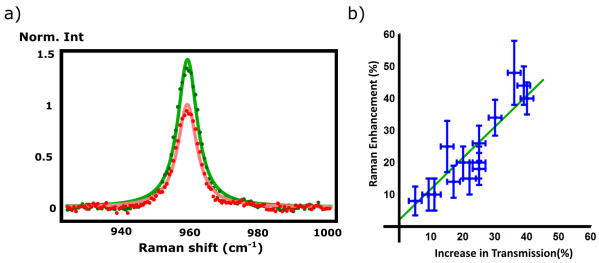

Fig. 4. a) Normalized spectral data points of the HAP peak collected in reflection before (red) and after (green) the wavefront optimization. Dots represent the experimental data and the solid lines, the Lorentzian fits to the data. The data in the figure corresponds to an enhancement in the Raman signal of 41%, which was achieved with an increase in total transmission of 39%. b) Increase of the Raman signal against the increase in the total pump transmission. It is possible to see how the data points follow a linear trend (in green) with a slope of 1.07 ± 0.12.

edges of the sample, i.e.

$$\left.\frac{I(z)}{L - z_R + z_{e2}}\right|_{z=z_R} = \left.\frac{I^{OP}(z)}{L - z_R^O + z_{e2}}\right|_{z=z_R^O} = \tan(\alpha). \tag{5}$$

Defining the distance $d = \left|z_R^O - z_R\right|$, and using the fact that $I^{OP}(z) = \beta I(z)$ we obtain

$$\frac{I(z_R)}{L - z_R + z_{e2}} = \frac{\beta I(z_R - d)}{L - z_R + z_{e2} + d}\,. \tag{6}$$

Solving Eq. (6) for d, we obtain that the extra distance at which a Raman element with the optimized intensity can be placed to generate the same measurable signal is given by:

$$\begin{aligned} d = {} & \frac{1}{2\beta}\left(\beta G - \frac{C}{L - z_R + z_{e2}}\right) \\ & + \frac{1}{2\beta}\sqrt{\left(\beta G - \frac{C}{L - z_R + z_{e2}}\right)^2 - 4\beta(C\,(1-\beta))} \end{aligned} \tag{7}$$

where $G = -L + z_{e1} - z_{e2} + 2z_R$ and $C = (z_R + z_{e1}) \cdot (L + z_{e2} - z_R)$.

In Fig. 5(b) we plot (on logarithmic scale) the normalized increase in the distance to the output surface ($d/(L - z_R)$), achieved by the extra pump intensity as a function of z_R. It is interesting to note that when the Raman element is around the central region of the sample, which in conventional approaches is the least accessible region [26], the optimized pump is capable of achieving an extra penetration depth between 30 and 100%. In Figs. 5(c) and 5(d) we represent the case where the signal of interest is scattered back from the medium, i.e. the backwards Raman emission. Figure 5(d) represents the equivalent case to Fig. 5(b) but when considering the Raman intensity collected in a reflection geometry, which leads to a very similar result. The study of the forward and backward Raman scattering (i.e. the transmitted or spatially collected light from the medium) are of interest for deep Raman spectroscopy given that both provide unique benefits for clinical applications [42].

6. Discussion

The technique presented and demonstrated in this work allows to increase the amount of pump energy density inside a scattering medium, thus increasing the amount of Raman signal produced

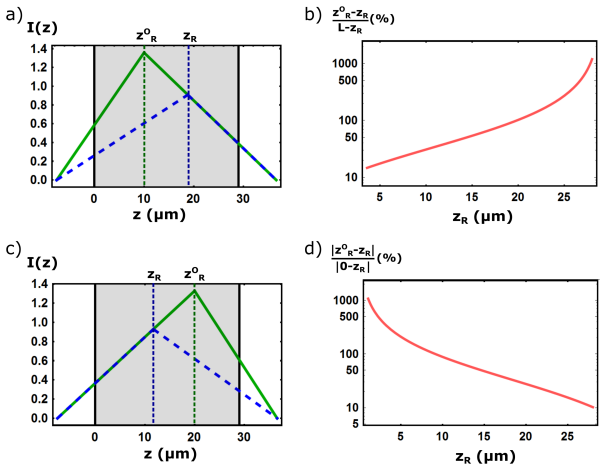

Fig. 5. a) Intensity distributions of Raman elements at two different positions giving rise to the same forward emission. The dashed blue curve represents the intensity distribution of a Raman element excited with a non-optimized pump at position z_R. The green curve represents the intensity distribution of a Raman element at a position z_R^O excited with an optimized pump (with 1.5 times higher intensity), farther away from the back-surface ($L = 29\mu m$), yet resulting in the same forward emission. b) Normalized increase in the distance at which an optimized Raman element would give rise to the same forward emission as a non-optimized one, dependent on the position of the Raman element (z_R). Note that the vertical axis is in logarithmic scale. c) Intensity distribution of the optimized and non-optimized Raman elements resulting in the same backward emission. d) Normalized increase in the distance at which the optimized Raman element should be in order to give the same backwards emission as the non-optimized emission.

by a sample buried deep inside it, without increasing the incident flux. As the optimization is done on the bright pump signal, each acquisition can happen on the time-scale of microseconds, as opposed to seconds or minutes for the Raman signal, so the optimization time is only limited by the 22 kHz rate at which the field can be modulated with the DMD. Although our proof-of-principle implementation currently takes approximately one hour to complete due to the computer-DMD data transfer bottleneck as well as several internal checks and diagnostic measures, the use of the DMD's field-programmable-gate-array (FPGA) would enable sub-second optimizations as demonstrated previously [14].

The transmission geometry used here was chosen for simplicity; however, there is no fundamental problem to implement the technique with spatially-offset Raman spectroscopy geometry [4, 5], thus facilitating the analysis of thick samples. The method is most suitable for incoherent Raman scattering. Although coherent anti-Raman spectroscopy (CARS) has been demonstrated with adaptive optics in turbid samples [43], the control of multiple wavelengths for CARS and stimulated Raman spectroscopy (SRS) does not readily translate to the highly scattering samples we considered in this study.

Absorption would make it more difficult to detect a signal coming from deep within the sample, even without the use of wavefront shaping [26, 44]. Nevertheless, provided that our approach is only based on the modification of the elastically scattered light, the pump signal can still be optimized to increase the energy density inside the scattering slab. When optimally coupling to the open channels, absorption would only lead to a slight modification of the intensity distribution inside the sample [39]. It should also be noted that the losses due to diffusion increase with sample thickness, while the optimal enhancement factor does not; it depends on the approximately

constant ratio of effective input and output modes, N_C/M_E. The iterative wavefront-shaping approach we adopted is highly tolerant to changes in the scattering matrix over time; however, it prevented us from reaching the theoretical enhancement limit. A complete transmission matrix measurement may be required to fully exploit the coupling between the output modes [34]. Alternatively, the number of controlled modes, N_C, can be increased to improve the enhancement factor further.

7. Conclusions

We have shown that the signal coming from a Raman active material buried deep inside a scattering medium can be enhanced by maximizing the total pump transmission via wavefront shaping. This is due to the fact that higher transmission modes store more energy inside the scattering medium than modes with low transmission [23]. By performing the wavefront shaping on the pump instead of the Raman signal, the process can be completed on a timescale much shorter than the Raman signal measurement itself [14]. We have shown experimentally an increase of 48% in the Raman signal in a well controlled and characterized system. These results show the potential of wavefront shaping techniques for enhancing the sensitivity of detection for biomedical applications such as the measurement of breast calcifications and bone quality using deep Raman approaches. We expect that this approach can enable even deeper readout of surface enhanced Raman scattering (SERS) labeled nanoparticles and surface enhanced spatial offset Raman spectroscopy (SESORS) [45].

Funding information

A. M. Paniagua-Diaz acknowledges support from EPSRC (EP/L015331/1) through the Centre of Doctoral Training in Metamaterials (XM2). A. Ghita and N. Stone contribution was funded by EPSRC [EP/P012442/1]. T. Vettenburg and J. Bertolotti acknowledges support from the Leverhulme Trust's Philip Leverhulme Prize. J. Bertolotti acknowledges support from the Leverhulme Trust (No. RPG-2016-129).

The research data supporting this publication are openly available from [46]

References

1. C. V. Raman and K. S. Krishnan, "A new type of secondary radiation," Nature **121**, 501 (1928).
2. P. Graves and D. Gardiner, *Practical Raman Spectroscopy* (Springer, 1989).
3. A. Mahadevan-Jansen and R. R. Richards-Kortum, "Raman spectroscopy for the detection of cancers and precancers," J. Biomed. Opt. **1**, 31–70 (1996).
4. P. Matousek and N. Stone, "Development of deep subsurface raman spectroscopy for medical diagnosis and disease monitoring," Chem. Soc. Rev. **45**, 1794–1802 (2016).
5. P. Matousek and N. Stone, "Emerging concepts in deep Raman spectroscopy of biological tissue," Analyst. **134**, 1058–1066 (2009).
6. A. Ghita, P. Matousek, and N. Stone, "Exploring the effect of laser excitation wavelength on signal recovery with deep tissue transmission Raman spectroscopy," The Analyst **141**, 5738–5746 (2016).
7. K. Kong, C. Kendall, N. Stone, and I. Notingher, "Raman spectroscopy for medical diagnostics: From in-vitro biofluid assays to in-vivo cancer detection," Adv. Drug Deliv. Rev. **89**, 121–134 (2015).
8. E. Akkermans and G. Montambaux, *Mesoscopic physics of electrons and photons* (Cambridge University., 2007).
9. I. M. Vellekoop and A. P. Mosk, "Focusing coherent light through opaque strongly scattering media," Opt. Lett. **32**, 2309 (2007).
10. A. P. Mosk, A. Lagendijk, G. Lerosey, and M. Fink, "Controlling waves in space and time for imaging and focusing in complex media," Nat. Photonics **6**, 283 (2012).
11. I. M. Vellekoop, E. Van Putten, A. Lagendijk, and A. Mosk, "Demixing light paths inside disordered metamaterials," Opt. Express **16**, 67–80 (2008).
12. J. V. Thompson, G. A. Throckmorton, B. H. Hokr, and V. V. Yakovlev, "Wavefront shaping enhanced Raman scattering in a turbid medium," Opt. Lett. **41**, 1769 (2016).
13. I. M. Vellekoop, "Feedback-based wavefront shaping," Opt. Express **23**, 12189–12206 (2015).
14. D. B. Conkey, A. M. Caravaca-Aguirre, and R. Piestun, "High-speed scattering medium characterization with application to focusing light through turbid media," Opt. Express **20**, 1733–1740 (2012).

15. J. X. Zhu, D. J. Pine, and D. A. Weitz, "Internal reflection of diffusive light in random media," Phys. Rev. A **44**, 3948–3959 (1991).
16. H. Yu, K. Lee, and Y. Park, "Energy leakage in partially measured scattering matrices of disordered media," Phys. Rev. B **93**, 104202 (2016).
17. R. Berkovits and S. Feng, "Correlations in coherent multiple scattering," Phys. Rep. **238**, 135 – 172 (1994).
18. J. F. de Boer, M. P. van Albada, and A. Lagendijk, "Transmission and intensity correlations in wave propagation through random media," Phys. Rev. B **45**, 658–666 (1992).
19. M. P. V. Albada and A. Lagendijk, "Observation of weak localization of light in a random medium," Phys. Rev. Lett. **55**, 2692–2695 (1985).
20. P.-E. Wolf and G. Maret, "Weak localization and coherent backscattering of photons in disordered media," Phys. Rev. Lett. **55**, 2696–2699 (1985).
21. C. W. J. Beenakker, "Random-matrix theory of quantum transport," Rev. Mod. Phys. **69**, 731 (1997).
22. O. Dorokhov, "On the coexistence of localized and extended electronic states in the metallic phase," Solid State Commun. **51**, 381–384 (1984).
23. W. Choi, A. P. Mosk, Q.-H. Park, and W. Choi, "Transmission eigenchannels in a disordered medium," Phys. Rev. B **83**, 134207 (2011).
24. M. Davy, Z. Shi, J. Park, C. Tian, and A. Z. Genack, "Universal structure of transmission eigenchannels inside opaque media," Nat. Commun. **6**, 6893 (2015).
25. M. Koirala, R. Sarma, H. Cao, and A. Yamilov, "Inverse design of perfectly transmitting eigenchannels in scattering media," Phys. Rev. B **96**, 054209 (2017).
26. M. Z. Vardaki, B. Gardner, N. Stone, and P. Matousek, "Studying the distribution of deep raman spectroscopy signals using liquid tissue phantoms with varying optical properties," Analyst **140**, 5112–5119 (2015).
27. A. Fick, "Uber diffusion," Poggendorff's Annalen der Physik und Cheimie **94**, 59 (1855).
28. O. S. Ojambati, H. Yilmaz, A. Lagendijk, A. P. Mosk, and W. L. Vos, "Coupling of energy into the fundamental diffusion mode of a complex nanophotonic medium," New J. Phys. **18** (2016).
29. M. Kim, Y. Choi, C. Yoon, W. Choi, J. Kim, Q.-H. Park, and W. Choi, "Maximal energy transport through disordered media with the implementation of transmission eigenchannels," Nat. Photonics **6**, 581–585 (2012).
30. W. Choi, M. Kim, D. Kim, C. Yoon, C. Fang-Yen, Q.-H. Park, and W. Choi, "Preferential coupling of an incident wave to reflection eigenchannels of disordered media," Sci. Rep. **5** (2015).
31. I. M. Vellekoop and A. P. Mosk, "Universal optimal transmission of light through disordered materials," Phys. Rev. Lett. **101**, 120601 (2008).
32. A. Goetschy and A. Stone, "Filtering random matrices: the effect of incomplete channel control in multiple scattering," Phys. Rev. Lett. **111**, 063901 (2013).
33. H. Yu, J.-H. Park, and Y. Park, "Measuring large optical reflection matrices of turbid media," Opt. Commun. **352**, 33–38 (2015).
34. C. W. Hsu, S. F. Liew, A. Goetschy, H. Cao, and A. Douglas Stone, "Correlation-enhanced control of wave focusing in disordered media," Nat. Phys. **13**, 497 (2017).
35. V. A. Marcenko and L. A. Pastur, "Distribution of eigenvalues for some sets of random matrices," Math. USSR-Sbornik **1**, 457–483 (1967).
36. S. L. Jacques, "Optical properties of biological tissues: a review," Phys. Medicine Biol. **58**, R37–R61 (2013).
37. T. Vo-Dinh, *Biomedical Photonics Handbook: Fundamentals, Devices and Techniques*, vol. 1 (CRC press, 2014).
38. I. M. Vellekoop and A. P. Mosk, "Phase control algorithms for focusing light through turbid media," Opt. Commun. **11**, 3071–3080 (2008).
39. R. Sarma, A. Yamilov, S. F. Liew, M. Guy, and H. Cao, "Control of mesoscopic transport by modifying transmission channels in opaque media," Phys. Rev. B **92**, 214206 (2015).
40. M. Mucalo, *Hydroxyapatite (HAp) for biomedical applications* (Elsevier, 2015).
41. J. Cheng and X. S. Xie, *Coherent Raman scattering microscopy* (CRC press, 2016).
42. S. Pahlow, K. Weber, J. Popp, B. R. Wood, K. Kochan, A. RÃijther, D. Perez-Guaita, P. Heraud, N. Stone, A. Dudgeon, B. Gardner, R. Reddy, D. Mayerich, and R. Bhargava, "Application of vibrational spectroscopy and imaging to point-of-care medicine: A review," Appl. Spectrosc. **72**, 52–84 (2018). PMID: 30265133.
43. A. J. Wright, S. P. Poland, J. M. Girkin, C. W. Freudiger, C. L. Evans, and X. S. Xie, "Adaptive optics for enhanced signal in cars microscopy," Opt. Express **15**, 18209–18219 (2007).
44. M. Z. Vardaki, P. Matousek, and N. Stone, "Characterisation of signal enhancements achieved when utilizing a photon diode in deep raman spectroscopy of tissue," Biomed. Opt. Express **7**, 2130–2141 (2016).
45. N. Stone, M. Kerssens, G. R. Lloyd, K. Faulds, D. Graham, and P. Matousek, "Surface enhanced spatially offset raman spectroscopic (sesors) imaging–the next dimension," Chem. Sci. **2**, 776–780 (2011).
46. http://doi.org/10.5281/zenodo.1319374.